

Insight on the Intracellular Supramolecular Assembly of DTTO: A Peculiar Example of Cell-Driven Polymorphism

Ludovico Aloisio, Matteo Moschetta, Alex Boschi, Ariel García Fleitas, Mattia Zangoli, Ilaria Venturino, Vito Vurro, Arianna Magni, Raffaello Mazzaro, Vittorio Morandi, Andrea Candini, Cosimo D'Andrea, Giuseppe Maria Paternò, Massimo Gazzano, Guglielmo Lanzani,* and Francesca Di Maria*

The assembly of supramolecular structures within living systems is an innovative approach for introducing artificial constructs and developing biomaterials capable of influencing and/or regulating the biological responses of living organisms. By integrating chemical, photophysical, morphological, and structural characterizations, it is shown that the cell-driven assembly of 2,6-diphenyl-3,5-dimethyl-dithieno[3,2-b:2',3'-d]thiophene-4,4-dioxide (DTTO) molecules into fibers results in the formation of a “biologically assisted” polymorphic form, hence the term bio-polymorph. Indeed, X-ray diffraction reveals that cell-grown DTTO fibers present a unique molecular packing leading to specific morphological, optical, and electrical properties. Monitoring the process of fiber formation in cells with time-resolved photoluminescence, it is established that cellular machinery is necessary for fiber production and a non-classical nucleation mechanism for their growth is postulated. These biomaterials may have disruptive applications in the stimulation and sense of living cells, but more crucially, the study of their genesis and properties broadens the understanding of life beyond the native components of cells.

1. Introduction


The spontaneous organization of small molecules into supramolecular structures is a ubiquitous process that implies a complex balance between several non-covalent interactions (i.e., hydrophobic interactions, hydrogen bonding, π - π interactions, and van der Waals forces). This process occurs in nature at all scales and underlies fundamental phenomena such as self-assembly and molecular recognition in fields ranging from materials science to biochemistry.^[1] In biological systems, supramolecular bioassemblies endowed with sophisticated functions are continuously created via a “bottom-up” fabrication process from different endogenous components.^[2] For example, lipids and proteins self-assemble to generate hierarchical nanostructures—such as actin filaments, microtubules, micelles, vesicles, membranes,

L. Aloisio, A. G. Fleitas, I. Venturino, A. Magni, C. D'Andrea, G. M. Paternò, G. Lanzani
Dipartimento di Fisica
Politecnico di Milano
Piazza L. da Vinci 32, Milano 20133, Italy
E-mail: guglielmo.lanzani@iit.it

L. Aloisio, M. Moschetta, A. G. Fleitas, I. Venturino, V. Vurro, A. Magni, C. D'Andrea, G. M. Paternò, G. Lanzani
Center for Nano Science and Technology
Istituto Italiano di Tecnologia
Via Rubattino 81, Milano 20134, Italy
A. Boschi
Center for Nanotechnology Innovation
Istituto Italiano di Tecnologia
Piazza S. Silvestro 12, Pisa 56127, Italy

M. Zangoli, A. Candini, M. Gazzano, F. Di Maria
Institute for Organic Synthesis and Photoreactivity (ISOF)
National Research Council of Italy (CNR)
Via P. Gobetti 101, Bologna I-40129, Italy
E-mail: francesca.dimaria@isof.cnr.it

R. Mazzaro
Dipartimento di Fisica e Astronomia “Augusto Righi”
Università di Bologna
Via C. Bertini Pichat 6/2, Bologna 40127, Italy
V. Morandi
Institute for Microelectronics and Microsystems (IMM)
National Research Council of Italy (CNR)
Via P. Gobetti 101, Bologna 40129, Italy

 The ORCID identification number(s) for the author(s) of this article can be found under <https://doi.org/10.1002/adma.202302756>

© 2023 The Authors. Advanced Materials published by Wiley-VCH GmbH. This is an open access article under the terms of the Creative Commons Attribution License, which permits use, distribution and reproduction in any medium, provided the original work is properly cited.

DOI: 10.1002/adma.202302756

etc.—essential for cellular functions.^[3] However, recent findings have shed light on the possibility of intracellular self-assembly of exogenous small molecules, namely cell-driven self-assembly, to affect/modulate cellular processes (such as apoptosis, replication, and signal transduction).^[4]

Most of the reported cell-driven self-assembled moieties are mainly based on biomolecules or derivatives such as small peptides, chlorophyll-based compounds, and natural biopolymers.^[5]

Recently, it was shown that another class of organic compounds, that is, thiophene-based oligomers, present the unique ability to assemble into fibrous supramolecular structures within living cells.^[6] Although several characterization techniques have been applied to reveal the constitution and formation mechanism of such fibers, a detailed picture is still lacking. What appears thrilling is that the formation of these fibers is specific to the cellular environment and cannot be reproduced in other simpler mediums. Indeed, 2,6-diphenyl-3,5-dimethyl-dithieno[3,2-b:2',3'-d]thiophene-4,4-dioxide (DTTO) aggregation readily occurs in certain solvents and in the solid state, albeit the morphology of the resulting structures differs from that of the fibers produced within cells. This suggests that the mechanism by which fibers are formed is intimately coupled to the cellular environment and, perhaps, the functioning routine.^[7] The formation of such fibers raises both fundamental chemical and biological questions. Understanding how simple components assemble to form highly ordered structures in living systems will enable us to directly build in vivo artificial electroactive constructs capable of conferring novel “bionic” features to cells and tissues. For instance, by utilizing DTTO self-assembling materials, it could be possible to create electroactive fibers that can serve as templates for tissue regeneration within the body. These structures can provide a scaffold for cell adhesion, proliferation, and differentiation while delivering precise electrical cues to guide and enhance the regenerative process.^[8] In addition, the capability of DTTO-based molecules to spontaneously penetrate the cell membrane offer a potential strategy to circumvent the brain–blood barrier and introduce bottom-up built molecular structures directly into the brain, providing new approaches to interface and manipulate the brain neural connections.^[9]

Here, we report a comprehensive characterization of the chemical, structural, optical, and electrical properties of cell-grown DTTO fibers, as well as of their formation process, by measuring the evolution of photoluminescence spectrum and dynamics in operando (i.e., during fibers formation within cells). This multi-characterization approach enabled us to identify the chemical composition of fibers and to gain insight into their growth within living cells. By complementing spectroscopic data with X-ray diffraction (XRD) characterization, we discovered an extended polymorphism of DTTO in the solid state, demonstrating that fibers are crystalline objects possessing a unique molecular arrangement. Cells induce a crystal form, that is, a biopolymorph, that cannot be replicated outside the cell. Notably, in recent years, general procedures for the formation of polymorphs have been reported, including sublimation, crystallization from a single solvent, evaporation from a binary mixture of solvents, vapor diffusion, thermal treatment, crystallization from the melt, growth in the presence of additives, and grinding, but none of them involve the out-of-equilibrium conditions present within living systems for the preparation of new organic materials.^[10]

Thus, the complex and dynamic environment within cells, characterized by continuously changing conditions (such as temperature, pH, and chemical composition), can provide novel routes for the assembly of organic materials. Our experimental observations suggest that: i) the aggregation occurring in living cells is restricted to the biotic phase, implying that the cellular machinery is involved, and ii) the formation of fibers takes place via a non-classical crystallization (NCC) route.^[11] Using conductive atomic force microscopy, we demonstrate that fibers have similar electrical conductivity to DTTO molecules deposited in thin films, indicating that fibers can retain their electrical characteristics after prolonged exposure/contact with the cells' aqueous environment. Finally, we demonstrate that crystalline fibers can “connect” cells by penetrating the plasma membrane of neighboring cells without killing them and can conform/adapt to cellular movement, indicating high fiber flexibility and potentially allowing for dynamic interactions and information exchange. What we show represents an innovative approach for creating unique cell-made conductive biomaterials, as well as a possible route for creating artificial gap-junctions between cells, potentially affecting signal propagation as seen in cardiomyocytes or, in general, affecting cell population behavior and environmental response.^[7,12]

2. Results and Discussion

2.1. In Vitro Growth of DTTO Fibers in C2C12 and HEK 293T Cells

Taking advantage of the intense green emission of DTTO molecules and resulting fibers, we tracked their formation and localization by confocal fluorescence microscopy (**Figure 1**).

During incubation, as shown in Figure 1A, DTTO molecules rapidly and spontaneously permeate the cellular membrane while remaining confined in the cytoplasm without penetrating the nucleus. The DTTO molecular uptake is regulated by diffusion through the cellular membrane. Indeed, inhibition of active endocytosis by treatment of cells with NaN_3 ^[13] does not affect the internalization of the molecule (see details in Figure S1, Supporting Information).

After internalization, DTTO molecules start forming globular clusters in the perinuclear region that act as seeds for the fiber's growth. Fibers are already visible one hour after treatment (Figure 1B) and continue to grow inside cells until they reach and pierce the plasma membrane without destroying it (Figure 1C). The intracellular growth of fibers and piercing of the plasma membrane does not alter cell viability; indeed, no evident cytotoxicity signs, including blebbing and cytosol spillover,^[14] are observed. To confirm this hypothesis, C2C12 cells were stained with propidium iodide (PI), a dye able to selectively stain the nucleus of dead cells. As shown in Figure S2 (Supporting Information), no PI was detected in cells with DTTO fiber piercing the membrane, suggesting no consistent cell membrane damage or disruption occurred. Using the same protocol in a different cell model, that is, HEK 293T, confirmed that fiber formation occurs in other cell lines and does not affect their viability and proliferation up to four days of incubation (Figures S3,S4, Supporting Information). Based on these observations and our previously published data,^[6,7] it can be inferred that the self-assembly

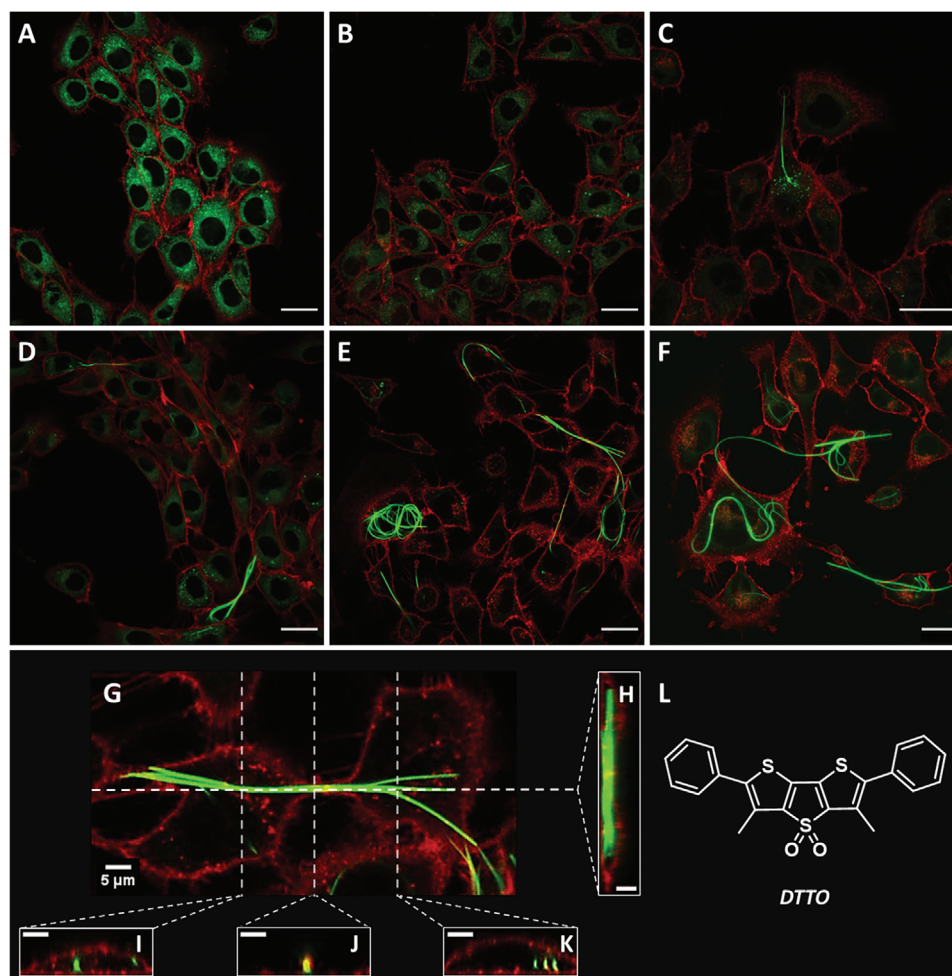


Figure 1. A–F) Laser scanning confocal microscopy (LSCM) images of C2C12 cells stained with DTTO, taken right after treatment (A), and B–F) 1 h (B), 3 h (C), 6 h (D), 12 h (E), and 24 h (F) after treatment. Cells were incubated with CellMask Deep Red plasma membrane stain for 5 min before imaging to highlight the cell membranes (red). All images are single planes of Z-stack acquisitions. Scale bar: 25 μ m. G) Orthogonal views of C2C12 cells 12 h after DTTO treatments. A single slice of Z-Stack. H) Section of Z-Stack cut along the fiber length. I–K) Section of Z-Stack cut along the corresponding vertical directions, orthogonal to the fiber. Scale bar: 5 μ m. L) DTTO molecular structure.

of DTTO into fibers is a universal phenomenon in living cells. Intriguingly, after membrane crossing, fiber growth appears to cease if the extracellular medium/cell interface is reached, whereas it continues if an adjacent cell is encountered, indicating that fiber synthesis and elongation require intracellular media (Figure 1D–F). Over time, this process culminates in forming a network of perfectly integrated fibers connecting multiple neighboring cells.

To better investigate the spatial positioning of the fibers in relation to the cells, Z-stacked images were acquired to reconstruct their 3D morphology. Figure 1G,H shows two orthogonal views, suggesting that fibers can extend from cell to cell and hence link them. Furthermore, Figure 1I outlines a third orthogonal direction, showing that fibers are within the perimeter of the membrane of a single cell, whereas Figure 1J,K confirms that fibers can cross the membrane between two adjacent cells, and can lie within the second cell. In physiological media mimicking intra or extracellular media, such as intracellular media (INTRA) and Krebs–Ringer–Hepes solution (KRH), Dulbecco’s modified Ea-

gle’s medium (DMEM) or aqueous solution (Figure S5, Supporting Information), similar fibers are not formed at all. This suggests that metabolic processes within living cells are the driving force behind fiber formation. Indeed, it has been previously reported that reducing cellular activity in vivo in Hydra by blocking protein translation results in a significant reduction in fiber formation.^[7]

2.2. Fibers Morphology and Composition

The morphology of isolated fibers was investigated ex situ by scanning electron microscopy (SEM), and the local elemental composition was determined by energy-dispersive spectrometry (EDS) mapping. **Figure 2** and Figure S6 (Supporting Information) illustrate the typical morphology of DTTO fibers, which exhibit either a flat rod-like morphology, that is, straight, or a twisted one, that is, helicoidal, within the same sample, with the latter being the predominant form. Helicoidal fibers exhibit a

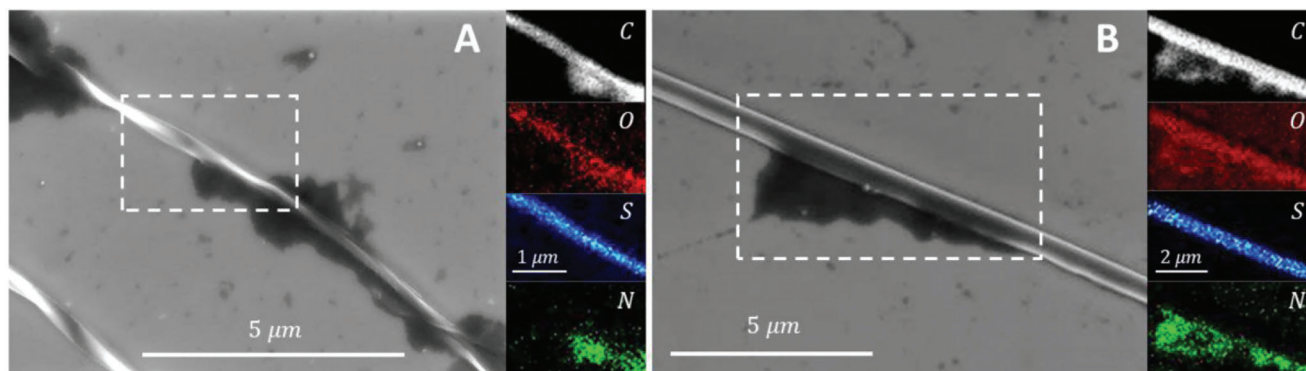


Figure 2. A,B) SEM images of DTTO fibers with different microstructures: A) helicoidal and B) straight, and corresponding EDS mapping of the selected area, highlighting the presence of a N-rich coating corresponding to the high contrast area on SEM images.

nanometric width (350 ± 100 nm) and micrometric length with a helical pitch of 3.9 ± 0.9 μm . The thickness of the fibers is estimated to be 100 ± 50 nm by measuring the spontaneously exposed transversal section of the fibers due to their helicoidal structure. Intriguingly, most of them consist of right-handed helices suggesting a possible influence of the chiral environment of the cell on DTTO supramolecular organization.^[15] Straight fibers present similar characteristics to helicoidal ones, although some of them display a reduced width. EDS revealed that both helicoidal (Figure 2A; Figure S7, Supporting Information) and straight (Figure 2B) fibers are mainly constituted of carbon and sulfur, with a small oxygen content related to the sulfoxide unit present in DTTO.

Most importantly, the absence of nitrogen-related signals suggests that DTTO fibers do not incorporate a significant amount of proteins, contrary to what was previously assumed.^[6a] Nevertheless, thin and high-contrast amorphous coatings usually adhere to fibers pointing out a specific superficial interaction between such structures. The high nitrogen content detected in these regions is clearly indicative of a protein-dominated composition, likely due to a non-specific protein coating forming a “corona” around fibers. Notably, this finding highlights the high affinity of proteins for fibers, probably owing to strong hydrogen bonding interactions involving the two oxygen atoms located on opposing sides of the plane of the heteroaromatic DTTO core. In addition, Raman microscopy performed on fibers and a thin film of DTTO deposited from CH_2Cl_2 for comparative purposes confirmed the EDS data. Indeed, the characteristic peaks of proteins, such as amide I ($1600\text{--}1690$ cm^{-1}) and amide III ($1290\text{--}1300$ cm^{-1}), are absent in both samples (Figure S8, Supporting Information), and only peaks relative to thiophene-based compounds, such as that the $\text{C}=\text{C}$ and $\text{C}-\text{C}$ stretching (1450 cm^{-1}),^[16] are present. These results confirm that DTTO molecules undergo self-assembly within living cells rather than being incorporated into intracellular protein structures.

2.3. Photophysics of DTTO in Different Aggregation States

The photophysical study of DTTO in different aggregation states enabled the elucidation of some key aspects concerning the structure, properties, and formation process of cell-fabricated DTTO

fibers. To this end, the absorption and emission properties of DTTO fibers were compared with those of i) a homogeneous solution of DTTO ($\text{DTTO}_{\text{DMSO}}$) in dimethyl sulfoxide (DMSO); ii) an aqueous suspension of DTTO (DTTO_{aq}) obtained by diluting $\text{DTTO}_{\text{DMSO}}$ in water; iii) a DTTO thin film prepared by drop casting from CH_2Cl_2 ($\text{DTTO}_{\text{film}}$).

As shown in Figure 3A, with respect to dissolved molecules in DMSO, the absorption spectrum of DTTO_{aq} shows a slight blueshift together with a broadening of the whole spectra, typical of structurally inhomogeneous aggregates. In contrast, measurements carried out on fibers and films show a stronger bathochromic shift, suggesting a dramatic change in the aggregation state and the intermolecular interaction.

Concerning the emission characteristics of these samples, as shown in Figure 3B, a redshift of the DTTO emission is observed moving from $\text{DTTO}_{\text{DMSO}}$, DTTO_{aq} (13 nm), DTTO fiber (16 nm), and $\text{DTTO}_{\text{film}}$ (25 nm), while the band shape remains virtually unchanged. In particular, fibers directly analyzed *in vivo* by time-resolved photoluminescence (TRPL) microscopy show a similar luminescence spectrum (PL) to DTTO_{aq} , indicative of the formation of DTTO supramolecular nanostructures driven by hydrophobic interactions (Figure 3C).^[17] On the other hand, fibers exhibit a lower PL quantum yield with respect to $\text{DTTO}_{\text{DMSO}}$ (30% vs 85%)^[18] but higher compared to its aggregated form in water and thin film, which are only 5% and 10% respectively (Figure S9, Supporting Information). This indicates that the aggregated states of DTTO_{aq} and $\text{DTTO}_{\text{film}}$ differ from that of the fibers.

It should be noted that the 1D topology in fibers favors radiative recombination with respect to film or aggregates.^[19] Consistently, the deactivation rates of the excited state (S_1) also change dramatically between these samples. In homogenous solutions, DTTO has a relatively long PL lifetime (≈ 10 ns), whereas, in water aggregates, the decay is considerably faster (≈ 1.5 ns). In thin films, the PL decay is even faster, ≈ 400 ps (Figure 3B). Fibers PL decay rate, however, is intermediate between DTTO_{aq} and $\text{DTTO}_{\text{film}}$ (≈ 800 ps), pointing to a unique supramolecular organization. It was observed that the PL decay kinetics of the fibers also have a long lifetime component. We hypothesize that this component originates from disordered segments along the fiber or small quantities of free DTTO that remain trapped near the fiber, perhaps in the protein wrapping some portions of

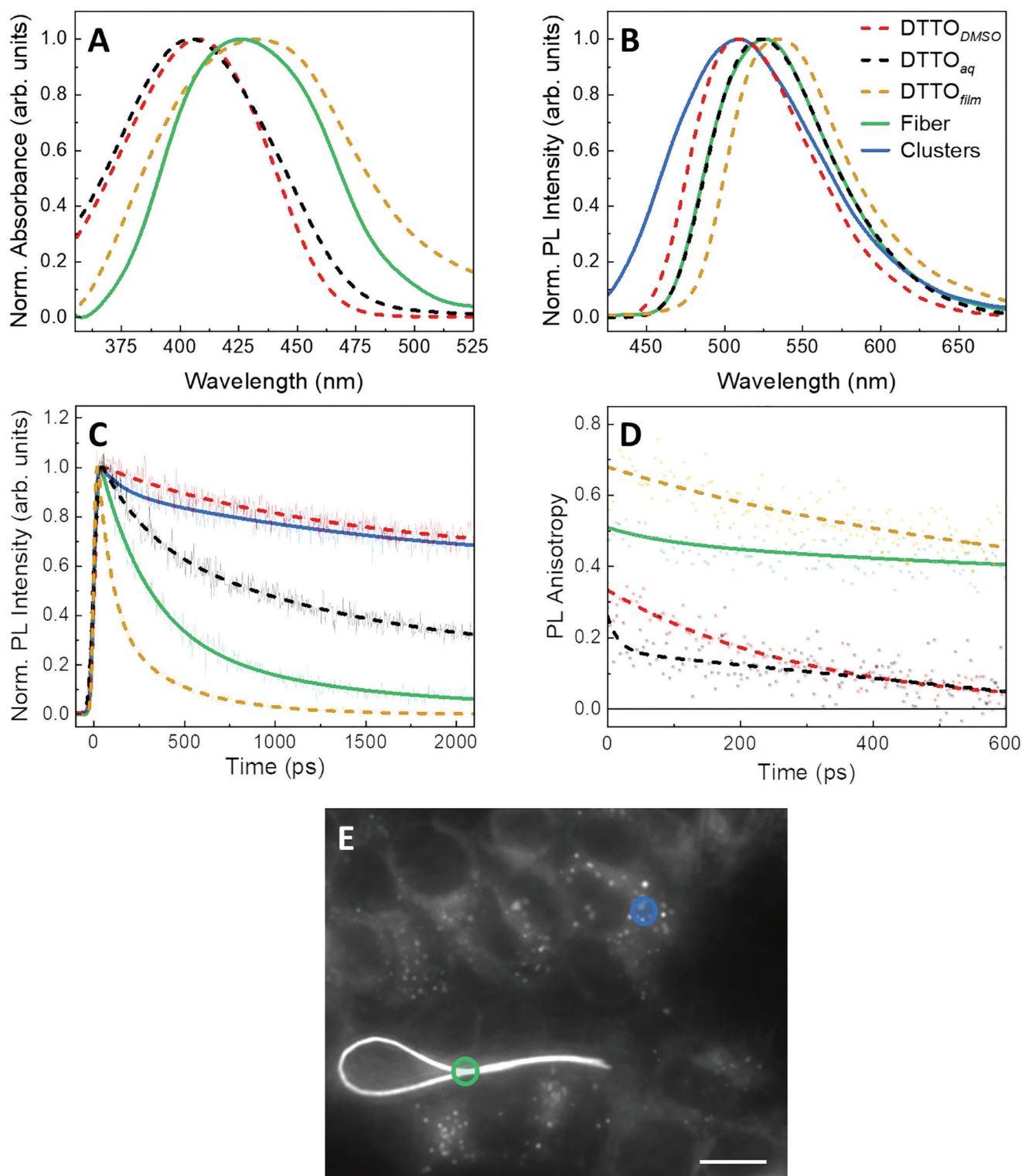


Figure 3. A) Absorbance spectra of DTTO in DMSO, water, thin film, and fibers. B) PL spectra (integrating for 2000 ps) of DTTO in different systems. Continuous lines are used for samples coming from living cells or fibers produced by living cells, dashed lines represent samples that do not involve cells. C) Double exponential fit of PL decays of DTTO's fluorescence signal integrated over the whole spectra. D) PL anisotropy decays of DTTO in the same systems, fibers were isolated from cells, purified, and deposited on a glass substrate to reduce signal from DTTO in cells. E) Fluorescence image obtained with TRPL microscopy setup, colored circles, highlight the spots analyzed and reported on the plots for fiber and cells without fiber. Scale bar: 25 μm.

the fibers. This speculation supports the idea that proteins play a role in the fiber formation process, acting as a template for further assembly.

For the considered samples, the radiative and non-radiative time constants result to be, respectively: $\text{DTTO}_{\text{DMSO}}$ ($\tau_{\text{R}} = 12.5$ ns $\tau_{\text{NR}} = 50$ ns), DTTO_{aq} ($\tau_{\text{R}} = 3$ ns $\tau_{\text{NR}} = 1.6$ ns), $\text{DTTO}_{\text{film}}$ ($\tau_{\text{R}} = 4$ ns $\tau_{\text{NR}} = 0.45$ ns), $\text{DTTO}_{\text{fiber}}$ ($\tau_{\text{R}} = 2.7$ ns $\tau_{\text{NR}} = 1.1$ ns). The radiative time is a quantum property of the system that stems from the ground and excited state wavefunction overlap (i.e., it depends on the square of the transition dipole moment). Clearly, thin film and fiber are comparable in this regard, whereas the water aggregate has a weakly allowed radiative transition, probably due to H-type molecular packing. Another property that can affect the radiative time is the molecular conformation: for cyclic molecules, the planar conformer generally has the shortest radiative time. This can explain the shorter value found in fibers and $\text{DTTO}_{\text{film}}$ with respect to $\text{DTTO}_{\text{DMSO}}$ (i.e., molecules are planar in film and fibers, twisted in solution).^[20] Non-radiative deactivation is due to several intrinsic and extrinsic causes that open up decay paths. Besides the molecular conformation mentioned above, it could be charge separation, trapping, acceptor centers in the system, or outside (solvent modes), whose efficiency depends on transport.^[21] It is interesting to note that these photophysical properties were not influenced by the helicoidal structure of fibers; indeed, no difference was found between helicoidal and straight fibers, probably because the helical pitch is too large with respect to the light absorption and emission wavelengths involved.

DTTO fibers were also investigated after their extraction from cells. The results indicate that neither the morphology nor PL spectra and lifetimes (Figure S10, Supporting Information) changed, indicating that the employed protocol does not affect the chemical–physical properties of the isolated fibers.

Photoluminescence anisotropy analysis has been carried out to better understand the supramolecular structure and the energy diffusion mechanisms (Figure 3D). In the DMSO solution, DTTO shows a behavior typical of isotropic systems; indeed, PL anisotropy right after the excitation is 0.32 (± 0.03), with relatively fast dynamics (268 ps) related to the rotational diffusion of DTTO molecules. Note that the initial anisotropy is lower than the theoretical value of 0.4, probably due to some deactivation already within the excitation pulse (IRF = 35 ps).^[22]

A similar anisotropy dynamic is found for aggregates in water (DTTO_{aq}), but the decay is much faster at the beginning due to energy transfer between randomly oriented molecules inside the aggregate. Once energy migration stops, having reached the localization threshold, rotation sets in, but due to the large aggregate inertial momentum, the dynamics slow down considerably, appearing as a linear decay in our time scale. In stark contrast, PL anisotropy in fibers and thin films starts from sensibly higher values, respectively 0.5 (± 0.03) for fibers and 0.68 (± 0.02) for $\text{DTTO}_{\text{film}}$ and displays a much slower decay. Both data indicate a crystalline order: excitation energy transfer does not significantly affect the emission polarization in ordered domains since it occurs between equally oriented molecules, thus with the same emission transition moment.^[23] The slower anisotropy decay in the fiber with respect to films highlights the even higher long-range spatial correlation in the latter. In (Figure S11, Supporting Information), we show that, as expected, the initial

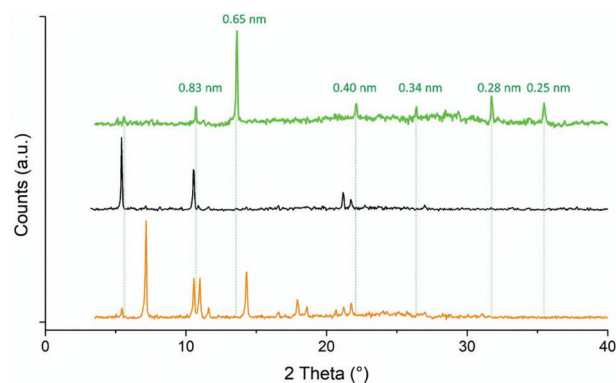


Figure 4. XRD patterns of scans obtained from fibers (green line), DTTO films from water (black line), and CH_2Cl_2 (orange line). The bell-shaped background due to the amorphous component of the support was subtracted. The dashed lines are a guide for the eye.

anisotropy value varies, changing the measured spot due to the random orientation of the crystalline axis in the macroscopic scale.

PL anisotropy also provides information regarding the orientation of monomers within the fibers. It is reasonable to assume that both the absorption and emission transition moments of DTTO are directed along its symmetry axis.^[24] Taking this into account, we measured the PL intensity of the same fiber spot when exciting with vertical and horizontal polarization. By considering the ratio of the two measurements, it is possible to estimate the direction of the absorption transition moment and, therefore, of the fluorophore and compare it to the fiber orientation. The DTTO dipole resulted to be always preferentially oriented along the direction of the fiber axis (Figure S12, Supporting Information), with a mean angle between the fiber orientation and absorption/emission transition moment of 22.5° . This indicates that the aggregation of DTTO occurs specifically along the growth direction of the fibers.

2.4. Structural Characterization of Fibers

Samples of DTTO fibers isolated from the cellular medium were subjected to XRD analysis to shed light on their structural organization. As depicted in Figure 4, the diffraction pattern of the fibers reveals several sharp peaks indicative of a well-organized crystalline material. Intriguingly, comparing the diffraction pattern of fibers to that of DTTO films deposited from CH_2Cl_2 or water reveals that fibers present a unique polymorphic structure. Polymorphism is a phenomenon commonly occurring in nature, and it is defined as the ability of a substance to organize itself into different crystalline structures (i.e., different arrangements of the molecules in the crystal lattice in terms of packing, orientation, or conformation).

As shown in Figure 4, all investigated samples present sharp diffraction peaks while possessing different XRD patterns proving the presence of different crystal phases. In particular, films from CH_2Cl_2 show the main peak at 7.05° corresponding to a periodicity of 1.25 nm, whereas films from water exhibit the main peak at 5.45° corresponding to a distance of 1.62 nm, indicating a different crystal phase. Intriguingly, fibers isolated from

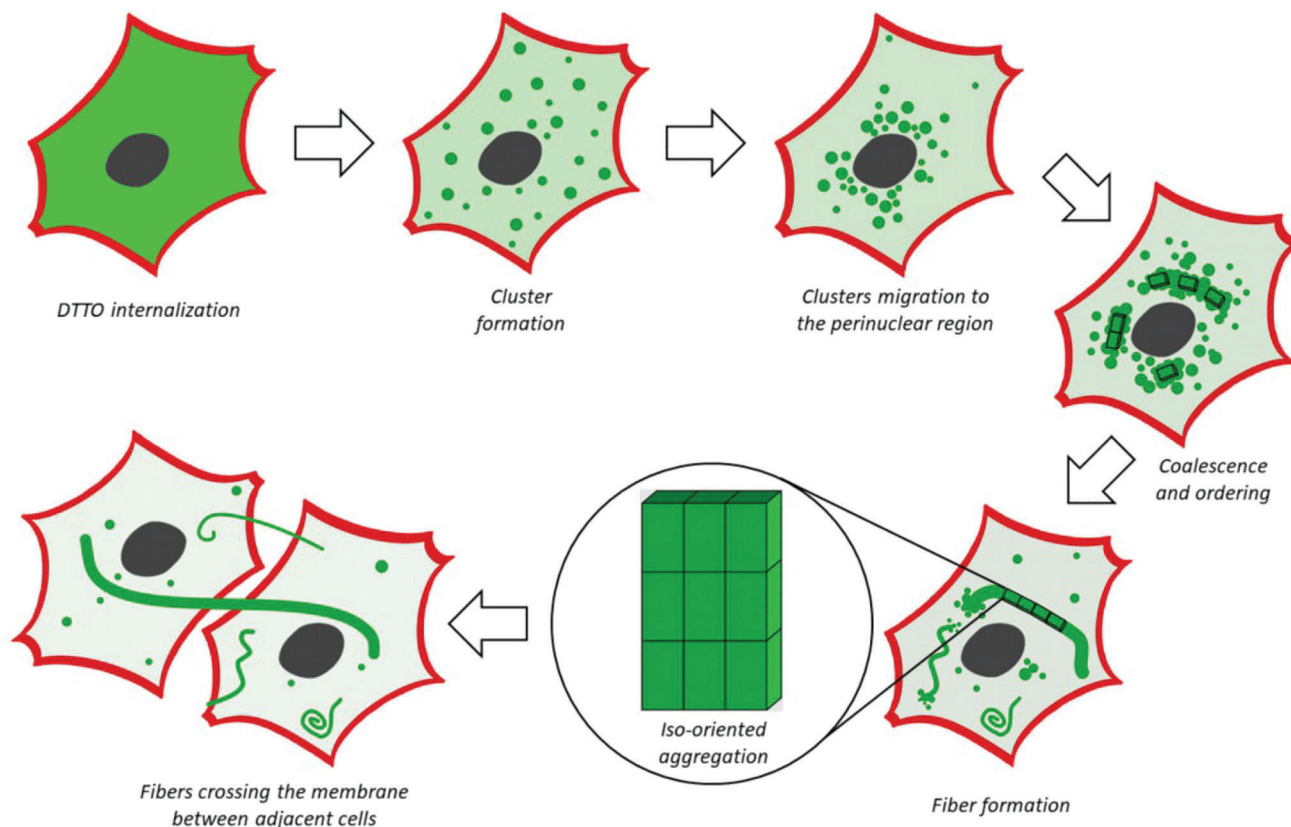


Figure 5. Proposed model representing the growth of crystalline fibers within living cells.

cells display high crystallinity but present a completely different diffraction pattern, with the most intense peak at 13.6° ($d = 0.65$ nm), proving a distinct molecular arrangement selectively induced by growth inside cells, in accord with spectroscopic analysis.

To investigate the origin of this polymorphism, we examined the crystallization behavior of DTTO in matrices that mimic intracellular and extracellular media, such as INTRA, KRH, and DMEM. Samples were prepared by dissolving DTTO in DMSO, injecting this solution into matrices of INTRA, KRH, and DMEM, and then depositing the resulting suspensions onto glass substrates.

As seen in Figure S13 (Supporting Information), the diffraction pattern of DTTO aggregates obtained in INTRA (i.e., intracellular media) and DMEM mimics those prepared in water; in fact, the most intense peak in both profiles is located at 5.45° . In contrast, the sample obtained in KRH (i.e., the extracellular media) has both peaks at 5.45° and 7.05° , showing that the specificity of the phase has been lost and that a mixture of polymorphs (i.e., those formed in film from CH_2Cl_2 and water) is present. It is important to note that despite the different compositions of these matrices (see Experimental Section), the aggregation of DTTO, which predominantly occurs instantaneously in these media, is not significantly influenced. These results confirm that the assembly of DTTO within the intracellular environment follows a distinct growth mechanism and takes place on a different time scale compared to its behavior in other non-biological matrices.

The different organization of DTTO aggregates in the tested matrices relative to fibers is further emphasized by the PL decays shown in Figure S14 (Supporting Information). Indeed, the PL decay rates of DTTO aggregates formed in these matrices are comparable to that observed in water. This suggests a common supramolecular arrangement of DTTO in these media distinct from that observed in cell-grown fibers, in agreement with XRD diffraction data.

According to real-time LSCM measurements, TRPL, and XRD data, we hypothesize that the fibers may grow through an NCC pathway involving the formation of liquid-like droplets during nucleation.^[11a-c] Nucleation is known to drive polymorph selection;^[10a,25] hence, the uniqueness of the cell-fabricated polymorph reflects the uniqueness of the conditions under which DTTO nucleation occurs, which cannot be reproduced in aqueous media or matrices mimicking intracellular environments. **Figure 5** schematizes the proposed growth process: after internalization, DTTO forms amorphous spherical clusters, ranging in size from 10 to 100 nm, by phase separation from the cytosol. Afterward, DTTO clusters accumulate, coalesce, and lead to the formation of fibrous crystals. The coalescence process proceeds only within the cellular matrix, even spanning multiple cells, but it is halted outside cells, despite the presence of DTTO in the extracellular solution. The process of fiber growth in HEK 293T cell treated with DTTO and stained with CellMask Deep Red is depicted in Video S1 (Supporting Information) through a series of Z-stack images from bottom to top. The video clearly shows that

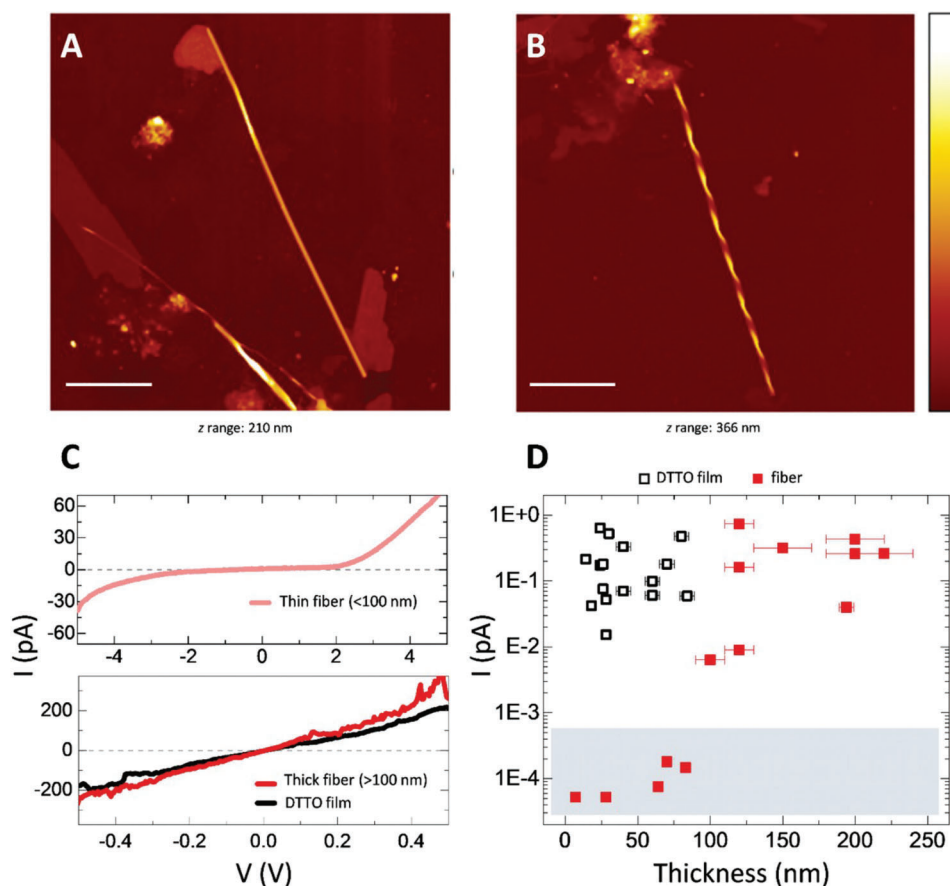


Figure 6. A,B) AFM topography images of representative straight and helicoidal fibers. Scale bars: 5 μm . C) PFTUNA local current vs voltage (I - V) curves acquired on a thin film (black curve, bottom) and on two representative fibers: pale red, top, for thin ($< \approx 10$ nm) fibers and red, bottom, for thick ($> \approx 100$ nm) fibers. D) PFTUNA current values measured at $V_{\text{bias}} = 500$ mV vs sample thickness for fibers (red squares) and thin film (black squares). The shaded area highlights current values comparable to the instrumental detection limit ($R > 10^{12} \Omega$).

the DTTO spherical clusters gather in a localized region, which turns out to be the growing edge of a fiber, confirming that the coalescence of these precursors is a crucial intermediate stage in cell-driven fiber formation.

2.5. Electrical Characterization of Fibers

The electrical properties of fibers were investigated by conductive atomic force microscopy (AFM) employing a Brukers Peak Force module (PFTUNA see Experimental Section), also allowing for the simultaneous measurement of the topography of the material. **Figure 6A,B** shows the topography of representative examples of DTTO fibers deposited on a gold substrate. The thickness of the fibers ranges from tens to hundreds of nanometers. Interestingly, the thin fibers (i.e., 10–100 nm) are exclusively straight with a uniform cross-section, whereas the thicker fibers (i.e., 100–300 nm) exhibit either a straight or helicoidal morphology (with helicoidal fibers dominating over straight fibers). Additionally, Figure S15 (Supporting Information) reports the topography of DTTO thin film deposited on a similar substrate from CH_2Cl_2 . The electrical properties of various types of fibers were investigated by measuring local $I(V)$ curves, using the conductive

tip of the probe as one electrode and the substrate as the other. **Figure 6C** compares two representative curves, one for fibers with a thickness greater than ≈ 100 nm (i.e., helicoidal or straight) and one for fibers with a thickness smaller than ≈ 100 nm (i.e., straight), to a typical curve measured on thin film. Fibers with a thickness greater than 100 nm present a linear conductive behavior strikingly comparable to that of the film. This result highlights that these bioassembled fibers retain their electrical characteristics despite the prolonged exposure/contact with the aqueous environment of the cells and the extraction and purification procedures. On the other hand, straight fibers with a thickness of less than ≈ 100 nm have a much higher resistance with non-linear characteristics, showing a detectable current signal only for relatively high voltage bias values (i.e., greater than a few volts, note the different x-axis scale for the two panels). This observation suggests the importance of the molecular packing and dimensionality of the resulting biomaterials for the appearance of charge carrier percolation pathways.

Figure 6D reports the current I probed at $V_{\text{bias}} = 500$ mV versus the sample thickness for a statistical distribution of fibers (both helicoidal and straight) and thin film. All measured current values for the thin film fall within the same region of the graph, indicating relatively uniform thickness and electrical properties.

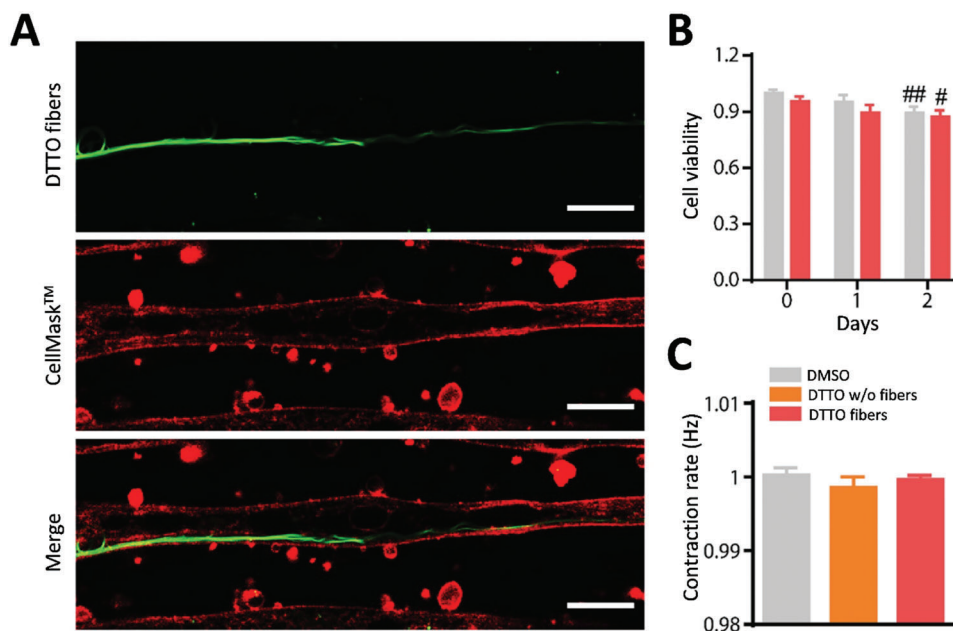


Figure 7. A) Representative confocal images of C2C12 myotubes stained with CellMask (red). DTTO fibers are represented in green. Scale bars: 25 μm . B) Normalized emission intensity at 600 nm (excitation wavelength: 546 nm) of AlamarBlue after reacting with cells for 4 h in complete DMEM. Emission measurements were taken by adding AlamarBlue at 0, 1, 2, 3, and 4 days after DTTO incubation. Data were normalized with respect to the average value of the DMSO samples of day 0 to evaluate cell viability. C) Data representing the contraction rate of C2C12 myotubes after 48 h of treatment with both DMSO and DTTOs. C2C12 myotubes with or without DTTO fibers were analyzed separately. Data are represented as mean \pm S.E.M. Viability: two-way ANOVA/Bonferroni's test; # $p < 0.05$; ## $p < 0.01$ within treatment with respect to day 0; $n = 12$ for each condition. Contraction rate: Kruskal–Wallis/Dunn's test; $p > 0.05$; $n = 42, 19,$ and 23 for DMSO, DTTO w/o fibers, and DTTO fibers, respectively.

On the contrary, the conductivity of the fibers markedly depends on the thickness. The current values measured in thinner fibers (i.e., $< \approx 100$ nm) always fall below 1 pA, comparable to our detection limit, while thicker fibers (i.e., $> \approx 100$ nm) show much higher values, similar to the ones found for the DTTO thin film. The fact that only the larger fibers exhibit good conductivity, similar to that of the cast film, suggests that with increasing the thickness, the effective coupling along the out-of-plane direction is enhanced; this can be attributed to the presence of highly ordered crystallites (similar to the ones present in the cast film) and/or the increase in crystallite size, in accordance with previous findings on another family of thiophene based derivatives.^[26]

2.6. C2C12 Myotubes Contraction

Fiber formation was further assessed on differentiated C2C12 myotubes to gain insights into their growth in a context that closely mimics muscle tissue. Myotubes were obtained starting from C2C12 myoblasts, which fuse together and differentiate into contractile cells. Myoblasts were seeded using the micro-contact printing technique to enhance their differentiation.^[27]

After reaching confluence, cells were allowed to differentiate for 8 days in DMEM containing 2% HS before being treated with DTTO.^[28]

As shown in **Figure 7A**, DTTO fibers are formed within the C2C12 myotubes; in particular, their growth occurs at a surprisingly higher rate than in other cell lines, and after 2 days, fibers

have already grown along the entire length of the myotube, reaching lengths of hundreds of micrometers (**Figure S16**, Supporting Information). This interesting aspect can be ascribed to the larger cell area of the C2C12 myotube, which could lead to a higher amount of internalized DTTO molecules. In addition, most of the fibers remain confined within cells, even after 48 h, probably due to the stiffer cell membrane of myotubes with respect to myoblasts. The viability of myotubes was assessed through AlamarBlue assay, and the results revealed no significant difference between cells loaded with DTTO and those treated with the vehicle (DMSO). It is important to note that after 2 days from the treatment, cell viability appears slightly reduced but independently from the treatment itself (**Figure 7B**), confirming that DTTO fibers formation does not compromise cellular integrity and activity.

It was found that the formation of fibers not only does not affect cell viability but also does not hinder their ability to contract. **Figure 7C** shows the contraction rate of myotubes triggered by an electric field. In this experiment, three different conditions were distinguished: i) DMSO (cells treated with the vehicle), ii) DTTO-treated cells in which fiber formation was observed, and iii) DTTO-treated cells in which fibers were not formed. Myotubes were stimulated by immersing two electrodes in the cell medium and applying a voltage of 3 V at a frequency of 1 Hz.^[29] As observed, no significant difference in contraction rate was spotted between the different conditions: all of them perfectly reproduce the frequency of the applied voltage pulses. This indicates that neither DTTO molecules nor fibers compromise their

capability to contract. Interestingly, contraction analysis revealed that the crystalline fibers are flexible enough to conform to the movement of the cells, as seen in Video S2 (Supporting Information) where a fiber “contracts” together with the myotubes that contain it.

As reported for C2C12 myoblasts, fibers eventually cross the myotube membrane ending up in the extracellular media and touching other cells (Figure S14, Supporting Information). Due to their electrical conductivity, DTTO fibers could be utilized to regulate the membrane potential of cells with unprecedented accuracy. By delivering a voltage to the end of DTTO fibers, for instance, it would be possible to control the activity of individual cells without coming into physical contact with them.^[30]

3. Conclusion

We have performed an in-depth analysis of the structural and physical properties of DTTO fibers bioassembled within living cells. By monitoring the fiber’s growth using LSCM, we observed that once the fibers reach a certain length within a cell, they are able to cross the plasma membrane, and in the presence of an adjacent cell, they continue to grow without harming either. In contrast, when the fiber reaches the extracellular solution, its growth is halted even in the presence of dispersed DTTO molecules. Hence, fiber growth results in the formation of a biomimetic and bio-inspired network interconnecting cells.

Combining photophysical, structural, morphological, and elemental characterizations, we demonstrate that fiber consists of close-packed DTTO molecules with proteins forming a “corona” around their surface. By exploring the aggregation of DTTO in different solvents or matrices mimicking the intra- and extracellular environment, we demonstrate that the peculiar way in which cells organize DTTO molecules cannot be reproduced outside living cells. These findings indicate that cellular activity plays a crucial role in fiber formation and that the intracellular species serve as a scaffold for the growth of DTTO fibers. Intriguingly, a detailed time-resolved microscopic investigation of fiber’s growth strongly supports an NCC mechanism for their formation. In fact, after internalization, DTTO is shown to form agglomerates in which the molecules are in a liquid-like phase prior to crystallization and formation of the ultimate fibrous structure. X-ray diffraction investigation demonstrates that fibers show high crystallinity and a distinct lattice structure compared to all other DTTO solid-state phases, proving that cells assemble DTTO into a bio-polymorph with unique morphological, optical, and electrical properties. This exciting finding opens the possibility of exploiting cellular systems for the uncovering of unreported polymorphs.

Our results highlight that DTTO fibers represent a promising scaffold for biomedical purposes since creating artificial electroactive constructs with defined morphology may confer novel “bionic” features to cells and tissue via temporally and spatially controlled stimulation. Furthermore, they can provide new approaches for directly linking the communication circuitry in a living system, for example, neural circuitry or muscle cell contraction signaling.

4. Experimental Section

Cell Culture Maintenance: In vitro experiments were performed using C2C12 (mouse myoblasts) and HEK 293T (human embryonic kidney) cells, purchased from ATCC. Cells were cultured in T-25 cell culture flasks containing Dulbecco’s modified Eagle medium high glucose (DMEM-HG) culture medium, supplemented with 10% heat-inactivated fetal bovine serum (FBS) and 1% GlutaMAX (0.5 mM, Invitrogen). Culture flasks were maintained in a humidified incubator at 37 °C with 5% CO₂. When at the confluence, cells were enzymatically detached from the flasks with a 1x trypsin-EDTA solution, plated on sterilized substrates, and left to grow for at least 24 h before performing the experiments. Prior to cell plating, a layer of fibronectin (2 μg mL⁻¹ in PBS buffer solution) was deposited on the sample surface and incubated for at least 1 h at 37 °C to promote cellular adhesion. For aligned cell plating, a micro-contact printing technique was used, as described in the next section.

C2C12 Seeding (Micro-Contact Printing) and Differentiation: Micropatterned substrates were prepared by stamping the PDMS on 18 mm round microscope glass slides coverslips. The PDMS stamp was coated with 200 μg mL⁻¹ of fibronectin (Sigma Aldrich) and let to rest for 60 min. The stamps were then dried with nitrogen and gently pressed on the substrate. After stamping the protein, the unpatterned regions of the substrate were blocked with 2% Pluronic F-127 (Sigma Aldrich) to render them non-adhesive to the cells. The substrate was rinsed three times with PBS before cell seeding. Approximately 18 000 cells cm⁻² were seeded on each substrate and incubated as reported in the “cell culture maintenance” section until confluence was reached. Twenty-four hours after reaching confluence, the cell growth medium was substituted with differentiation medium (DMEM-HG culture medium, supplemented with 2% heat-inactivated horse serum (HS) and 1% GlutaMAX) and incubated for 10 days to induce myotube formation. Differentiation media exchanges were performed every 48 h.

DTTO Treatment: C2C12 cells were seeded at a density of ≈12 000 cells cm⁻² in a 12-well tissue culture plate in 1 mL of complete culture medium per well. DTTO was dissolved in DMSO at a concentration of 2.5 mg mL⁻¹ to obtain a stock solution and then was diluted in DMEM to the final concentration of 25 μg mL⁻¹ before adding it to the cells. Cells were then incubated at 37 °C in 5% CO₂, 95% relative humidity for 1 h. After the incubation time, the remaining dye in the solution and DTTO aggregated, which did not penetrate the cell membrane, were washed with PBS before performing each experiment.

Uptake Assay: For this experiment, 50 000 cells cm⁻² were plated on a 24-multiwell plate 24 h before the investigation. On the day of the experiment, half of the samples were incubated with 10 μg mL⁻¹ of Na₃ for 1 h to block active endocytosis. After the treatment, cells were loaded with DTTOs as previously described. After the loading, cells were washed with PBS and resuspended in NaOH 1 M. The DTTO fluorescence was detected using a fluorescence spectrophotometer, exciting at 403 nm and measuring the emission at 530 nm.

Viability Assay: To assess DTTO biocompatibility, an AlamarBlue proliferation assay was performed. The toxicity assay with AlamarBlue was an indirect method based on the quantitative measurement of cellular metabolic activity by measuring fluorescence. Resazurin, the active principle in the AlamarBlue reagent, was a non-fluorescent and non-toxic compound permeable to the cell membrane. Viable cells reduce Resazurin to Resofurin, a highly fluorescent compound. The conversion from the oxidized to the reduced form caused an absorption shift from 600 to 570 nm. For this experiment, 4000 cells cm⁻² were plated 24 h before the experiment (for HEK-293T cells), or 18 000 cells cm⁻² were plated and induced to differentiate as reported previously (for myotubes). After 8 days of exposure to the differentiation medium, DTTO was incubated with cells for 1 h. After AlamarBlue reagent (Invitrogen DAL 1100) was diluted 1:10 with DMEM without phenol red. The solution without the cell was used as blank. The samples were incubated for 4 h (for HEK-293T cells) or 2 h (for myotubes) and, subsequently, a 100 μl aliquot of the solution was removed from each well and transferred to a 96-well plate. The fluorescence was detected using a fluorescence spectrophotometer, exciting at 560 nm and measuring the emission at 590 nm. The emission value was acquired

3 times per aliquot to obtain a reliable measure. Cells were monitored until 2 days. The day before DTTO treatment, an additional assay was performed on each well to assess the viability of the untreated myotubes. The emission values were then normalized with respect to the values of the untreated cells corresponding to the same well.

Statistical Analysis: Data were expressed as mean \pm standard error of the mean (S.E.M.) or box plots. Normal distribution was assessed using D'Agostino and Pearson's normality test. To compare multiple variables, the two-way analysis of variance (ANOVA) test with Bonferroni's correction was used. To compare more than two distinct groups with one single variable one-way ANOVA test was used with normally distributed data, while Kruskal–Wallis test with Dunn's multiple comparison tests was used for non-normally distributed groups. To compare two distinct groups with one single variable Student's *t*-test was used with normally distributed data, while Mann–Whitney *U*-test was used for non-normally distributed groups. The significance level was preset to $p < 0.05$ for all tests. Statistical analysis was carried out using Prism 6 (GraphPad Software, Inc.).

Confocal Imaging: For confocal imaging, an inverted confocal laser microscope, Nikon Eclipse Ti2, was used. The acquisition was performed with NIS-Element, Nikon Imaging Software. For the localization experiments, 12 000 cells cm^{-2} were plated 24 h before the experiment. On the day of the experiments, cells were incubated with DTTOs for 1 h. After the incubation, samples were washed with PBS to remove cell unbound molecules. Myotubes were differentiated and treated with DTTO, as reported in the previous sections. Next, samples were incubated for 5 minutes with CellMask Deep Red (Thermo Fisher) plasma membrane stain to detect cell plasma membrane. Samples were washed with PBS, and the acquisition was performed using a 60 \times objective for cell Z-stack acquisition of consecutive confocal sections. Hoechst, DTTO, propidium iodide, and CellMask were excited using 403.3 nm (detection channel 425–475 nm and 500–550 nm), 561 nm (collection channel 570–620 nm), and 640 nm (collection channel 663–743 nm) lasers, respectively. The acquired images were analyzed with Fiji (ImageJ).

Propidium Iodide Staining: Twelve-thousand cells per cm^2 were plated 24 h before the experiment. 24 h before the experiment, cells were incubated with DTTOs for 1 h, as reported previously. Before imaging, samples were incubated for 5 min with CellMask Deep Red (Thermo Fisher) plasma membrane stain, propidium iodide, and Hoechst. The acquisition was performed using a 60 \times objective for cell Z-stack acquisition of consecutive confocal sections. DTTO, PI, and CellMask were excited using 403.3 nm (collection channel 500–550 nm), 561 nm (collection channel 590–630 nm), and 640 nm (collection channel 663–743 nm) lasers, respectively.

DTTO Fiber Harvesting: Fibers were isolated from cells similar to what was already reported by Palamà et al.^[6a] DTTO fibers were purified by whole cell lyses in 50 mM Tris HCl, pH 7.4; 1% Triton X-100; 5 mM EDTA; 150 mM NaCl; 1 mM Na_3VO_4 ; 1 mM NaF; 1 mM PMSF; 10 μM benzamidin-HCl; 10 $\mu\text{g mL}^{-1}$ aprotinin; 10 $\mu\text{g mL}^{-1}$ leupeptin; 10 $\mu\text{g mL}^{-1}$ pepstatin A. The resulting solution was then washed multiple times with fresh lysis buffer by centrifugation (1550 rpm, 20 min, 4 °C) and stored at -80 °C for further use.

Relative PL Quantum Yield: PL quantum yield was measured for the previously analyzed samples at different excitation powers (0.5, 1, 5, and 10 mW) following the protocol reported by de Mello et al.^[31] Relative PL quantum efficiency was then established by averaging the measured values and normalizing them with respect to DTTO in DMSO, which had the maximum efficiency between the measured samples.

Time-Resolved Photoluminescence (TRPL): TRPL measurements were carried out using Ti: Sapphire laser source (Chameleon Ultra II, Coherent, producing pulses of 140 fs with a repetition rate of 80 MHz). Second harmonic generation was obtained using a barium borate crystal; two BG40 filters were used to remove residuals of the fundamental. The excitation beam (405 nm) was reflected off a suitably chosen dichroic mirror (LP425) before hitting the sample. The emission was collected with an Acton SP2300i, Princeton Instrument spectrograph coupled with a Hamamatsu C5680 streak camera with the Synchroscan sweep module. The streak image was recorded by a Hamamatsu ORCA-R2 C10600 CCD. The measurements recorded the first 2 ns of decay, with a temporal resolution

of ≈ 20 ps. For measurements on living cells and isolated fibers (TRPL microscopy), the excitation beam was collected into a 63 \times water immersion objective (for living cells) or 40 \times objective (for the other measurements) and focused onto the sample to achieve spatial resolution, obtaining an excitation spot diameter of 1 μm and a power of 2 μW . The microscope field was visualized using a flip mirror and a CMOS camera (ORCA-Flash 2.8, Hamamatsu), allowing the accurate focus of the excitation beam on the sample with the help of a sample XYZ differential micrometer translation stage. The emission signal was focused on the entrance slit of the spectrograph, as previously described.

PL Anisotropy Calculation: PL anisotropy over time was calculated according to the definition $r = (I_{\parallel} - GI_{\perp}) / (I_{\parallel} + 2GI_{\perp})$, where I is the intensity of the PL signal (parallel or orthogonal to the excitation beam), and G is a correction factor that takes into account different sensitivities of the detector to orthogonally polarized signals.^[32] The correction factor G was calculated assuming that the PL anisotropy of small molecules in good solvents, which could easily rotate and reorient randomly, should tend to 0.^[21b] Accordingly, the correction factor G to have $r(\infty) = 0$ in DMSO resulted to be 0.868.

Scanning Electron Microscopy (SEM) Analysis: Field-emission scanning electron microscopy was performed on Zeiss LEO 1530 FE-SEM equipped with X-act - 10 mm² SDD EDS Detector by Oxford Instruments. Images were collected operating at $V_{\text{acc}} = 5$ keV. The samples were drop-cast onto Si/SiO₂ wafers and dried under vacuum with no further treatment.

X-ray Diffraction (XRD) Measurements: XRD patterns of purified powder samples and drop-cast films were recorded by means of a PANalytical X'PertPro diffractometer equipped with a fast, solid-state X'Celerator detector and a copper target ($\lambda = 0.15418$ nm). The samples were scanned in the range $2\theta = 3.2^\circ$ to 40° (step size of 0.033° , acquisition time of 200 s per step).

Atomic Force Microscopy (AFM) and Peak-Force Tuna (PFTUNA) Microscopy: All scanning probe microscopy characterizations were performed in the air with a Bruker Multimode 8 microscope. Fiber samples for SPM were prepared by drop-casting 10 mL of fiber suspended in water on fresh gold on mica substrates (Phasis, CH). For comparison, DTTO dissolved in tetrahydrofuran (2.5 mg mL^{-1}) was also drop-cast on the same type of substrates. Employing Bruker's PFTUNA mode, it was possible to simultaneously measure topography, mechanical properties (i.e., adhesion), and the electrical current passing from the substrate to the tip through the sample, with a detection limit below 1 pA. Local current–voltage (I – V) curves were acquired by keeping the tip at a fixed position and ramping the voltage bias. Each plotted curve/measured $I(V)$ value was obtained after averaging three consecutive measurements. Bruker “SCM-PIT-V2” probe ($f = 75$ kHz, $k = 3$ N m^{-1} , material: n-Si) was used for all the measurements. The processing and analysis of the scanning probe images for correcting piezo-scanner artifacts were performed using SPIP software.

DTTO Aggregation in Physiological Media Mimicking Intra or Extracellular Media: DTTO was dissolved in DMSO at a concentration of 2.5 mg mL^{-1} ; then 0.25 μL of this solution was injected into three different matrices: INTRA (12 mM KCl, 125 mM K-Gluconate, 1 mM MgCl_2 , 0.1 mM CaCl_2 , 10 mM EGTA, 10 mM Hepes, 10 mM ATP), KRH (Krebs–Ringer–Hepes solution: 135 mM NaCl, 5.4 mM KCl, 1 mM MgCl_2 , 1.8 mM CaCl_2 , 5 mM Hepes), DMEM complete (Dulbecco's modified Eagle's medium, 10% fetal bovine serum, 1% GlutaMAX).

Contraction Experiments: C2C12 cells were differentiated as previously reported, and myotubes were treated with DTTO 2 days before the experiment. Cells were placed in the extracellular solution (NaCl 0.14 M, KCl 5.4 mM, MgCl_2 1.8 mM, CaCl_2 1.8 mM, Glucose 11 mM, and HEPES 10 mM). Nikon Eclipse Ti inverted microscope, coupled with a 20 \times /0.50 objective purchased from Nikon was used to stimulate the cells. The electrical stimulation was achieved by applying 20 ms pulses of voltage (3 V) at a frequency of 1 Hz. The effect of electrical stimulation was recorded using PVCam software, starting the stimulation 10 s after the beginning of the video, and stopping the recording after several seconds at the end of the protocol to distinguish spontaneous contractions from the effect of the applied voltage. All the measurements were performed at room temperature.

Video Analysis: The single frames of the videos recorded by PVCam software were put together with Fiji (ImageJ) software and analyzed with MATLAB code. The code was based on a visual recognition algorithm that allowed to characterize the movement of an object, chosen by the user, through each frame. The code was based on Kanade–Lucas–Tomasi algorithm.^[33] The selected ROI was divided into indifferent subregions, each with its coordinates. This allowed evaluating the average displacement of each point from its zero, allowing us to obtain the average contraction path of a contracting myotube. The frequency of contraction was obtained by evaluating the distance between two consecutive peaks from the contraction profile curve (displacement over time). A series of optimization of the code were employed to reduce noise and correctly highlight the single contraction peak (i.e., minimum value, a minimum distance between two peaks, etc.). Then the mean contraction time and frequency were evaluated for each myotube.

Supporting Information

Supporting Information is available from the Wiley Online Library or from the author.

Conflict of Interest

The authors declare no conflict of interest.

Author Contributions

L.A., M.M., and A.B. contributed equally to this work. The manuscript was written through the contributions of all authors. All authors had given approval to the final version of the manuscript.

Data Availability Statement

The data that support the findings of this study are available in the supplementary material of this article.

Keywords

biomaterials, electroactive fibers, polymorphs, supramolecular assembly, thiophene

Received: March 24, 2023

Revised: June 7, 2023

Published online: August 17, 2023

- [1] a) J. M. Lehn, *Chem. Soc. Rev.* **2007**, *36*, 151; b) G. Bellapadrona, M. Elbaum, *Angew. Chem., Int. Ed.* **2014**, *126*, 1560; c) J. M. Lehn, *Proc. Natl. Acad. Sci. USA* **2002**, *99*, 4763; d) J. M. Lehn, *Supramolecular Chemistry: Concepts and Perspectives*, Wiley-VCH, Weinheim, Germany **1995**; e) A. D. Q. Li, *Molecular Self-Assembly: Advances and Applications*, Pan Stanford Publishing, Singapore **2012**; f) J. Kosco, F. Moruzzi, B. Willner, I. McCulloch, *Adv. Energy Mater.* **2020**, *10*, 2001935; g) F. Di Maria, M. Zangoli, G. Barbarella, *Org. Mater.* **2021**, *3*, 321; h) K. Das, L. Gabrielli, L. J. Prins, *Angew. Chem., Int. Ed.* **2021**, *60*, 20120; i) T. Kato, M. Yoshio, T. Ichikawa, B. Soberats, H. Ohno, M. Funahashi, *Nat. Rev. Mater.* **2017**, *2*, 17001.
- [2] a) F. Sheehan, D. Sementa, A. Jain, M. Kumar, M. Tayarani-Najjaran, D. Kroiss, R. V. Ulijn, *Chem. Rev.* **2021**, *121*, 13869; b) P. J. Cragg, *Supramolecular Chemistry*, 1st ed., Springer, **2010**; c) B. J. G. E. Pieters, M. B. van Eldijk, R. J. M. Nolte, J. Mecnović, *Chem. Soc. Rev.* **2016**, *45*, 24.
- [3] a) L. E. Bickerton, T. G. Johnson, A. Kerckhoffs, M. J. Langton, *Chem. Sci.* **2021**, *12*, 11252; b) M. Dergham, S. Lin, J. Geng, *Angew. Chem., Int. Ed.* **2022**, *61*, e202114267.
- [4] a) H. Wang, Z. Feng, B. Xu, *Chem. Soc. Rev.* **2017**, *46*, 2421; b) M. Pieszka, S. Han, C. Volkmann, R. Graf, I. Lieberwirth, K. Landfester, D. Y. W. Ng, T. Weil, *J. Am. Chem. Soc.* **2020**, *142*, 15780; c) M.-Z. Zhao, D.-B. Cheng, Z.-R. Shang, L. Wang, Z.-Y. Qiao, J.-P. Zhang, H. Wang, *Chinese J. Polym. Sci.* **2018**, *36*, 1103; d) Y. Hou, L. Zou, Q. Li, M. Chen, H. Ruan, Z. Sun, X. Xu, J. Yang, G. Ma, *Mater. Today Bio* **2022**, *15*, 100327; e) H. Wang, Z. Feng, B. Xu, *Angew. Chem., Int. Ed.* **2019**, *58*, 10423.
- [5] a) J. Q. Cai, X.-M. Liu, Z. J. Gao, L. L. Li, H. Wang, *Mater. Today* **2020**, *45*, 77; b) S. F. Shimobayashi, P. Ronceray, D. W. Sanders, M. P. Haataja, C. P. Brangwynne, *Nature* **2021**, *599*, 503; c) Y. Pei, L. Wang, K. Tang, D. L. Kaplan, *Adv. Funct. Mater.* **2021**, *31*, 2008552.
- [6] a) I. E. Palamà, F. Di Maria, I. Viola, E. Fabiano, G. Gigli, C. Bettini, G. Barbarella, *J. Am. Chem. Soc.* **2011**, *133*, 17777; b) I. Viola, I. E. Palamà, A. M. L. Coluccia, M. Biasiucci, B. Dozza, E. Lucarelli, F. Di Maria, G. Barbarella, G. Gigli, *Integr. Biol.* **2013**, *5*, 1057; c) I. E. Palamà, F. Di Maria, S. D'Amone, G. Barbarella, G. Gigli, *J. Mater. Chem. B* **2015**, *3*, 151; d) I. E. Palamà, G. Maiorano, F. Di Maria, M. Zangoli, A. Candini, A. Zanelli, S. D'Amone, E. Fabiano, G. Gigli, G. Barbarella, *ACS Omega* **2022**, *7*, 12624.
- [7] M. Moros, F. Di Maria, P. Dardano, G. Tommasini, H. Castillo-Michel, A. Kovtun, M. Zangoli, M. Blasio, L. De Stefano, A. Tino, G. Barbarella, C. Tortiglione, *iScience* **2020**, *23*, 101022.
- [8] a) E. Uliassi, L. E. Peña-Altamira, A. V. Morales, F. Massenzio, S. Petralla, M. Rossi, M. Roberti, L. Martinez Gonzalez, A. Martinez, B. Monti, M. L. Bolognesi, *ACS Chem. Neurosci.* **2019**, *10*, 279; b) A. J. Russell, *ACS Med. Chem. Lett.* **2013**, *4*, 365; c) L. Silpa, R. Sim, A. J. Russell, *Bioorg. Med. Chem. Lett.* **2022**, *61*, 128601; d) D. Cao, J. Ding, *Regener. Biomater.* **2022**, *9*, rbac098.
- [9] a) R. Daneman, A. Prat, *Cold Spring Harb. Perspect. Biol.* **2015**, *7*, a020412; b) C. M. Bellettato, M. Scarpa, *Ital. J. Pediatr.* **2018**, *44*, 131; c) S. Ding, A. I. Khan, X. Cai, Y. Song, Z. Lyu, D. Du, P. Dutta, Y. Lin, *Mater. Today* **2020**, *37*, 112.
- [10] a) M. R. Caira, in *Handbook of Thermal Analysis and Calorimetry*, Vol. 5, 2nd ed. (Eds: S. Vyazovkin, N. Koga, C. Schick), Elsevier, Amsterdam, The Netherlands **2008**, Ch. 5; b) E. H. Lee, *Asian J. Pharm. Sci.* **2014**, *9*, 163; c) A. J. Cruz-Cabeza, N. Feeder, R. J. Davey, *Commun. Chem.* **2020**, *3*, 142.
- [11] a) H. Fu, X. Gao, X. Zhang, L. Ling, *Cryst. Growth Des.* **2022**, *22*, 1476; b) Y. Tsarfaty, S. Rosenne, H. Weissman, L. J. W. Shimom, D. Gur, B. A. Palmer, B. Rybtchinski, *ACS Cent. Sci.* **2018**, *4*, 1031; c) M. Jehannin, A. Rao, H. Cölfen, *J. Am. Chem. Soc.* **2019**, *141*, 10120; d) J. L. Perez Velazquez, P. L. Carlen, *Trends Neurosci.* **2000**, *23*, 68.
- [12] N. Kudryashova, A. Nizamieva, V. Tselaya, A. V. Panfilov, K. I. Agladze, *PLoS Comput. Biol.* **2019**, *15*, 1006597.
- [13] R. D. Klausner, J. Van Renswoude, G. Ashwell, C. Kempf, A. N. Schechter, A. Dean, K. R. Bridges, *J. Biol. Chem.* **1983**, *258*, 4715.
- [14] X. Hu, Z. Li, R. Lin, J. Shan, Q. Yu, R. Wang, L. Liao, W. Yan, Z. Wang, L. Shang, Y. Huang, Q. Zhang, K. Xiong, *Front. Cell Dev. Biol.* **2021**, *9*, 634690.
- [15] a) N. E. Shepherd, H. N. Hoang, G. Abbenante, D. P. Fairlie, *J. Am. Chem. Soc.* **2009**, *131*, 15877. b) Y. Sang, M. Liu, *Chem. Sci.* **2022**, *13*, 633.
- [16] a) A. Brillante, I. Bilotti, F. Biscarini, R. G. Della Valle, E. Venuti, *Chem. Phys.* **2006**, *328*, 125; b) F. Di Maria, E. Fabiano, D. Gentili, M. Biasiucci, T. Salzillo, G. Bergamini, M. Gazzano, A. Zanelli, A. Brillante, M. Cavallini, F. D. Sala, G. Gigli, G. Barbarella, *Adv. Funct. Mater.* **2014**, *31*, 4943.
- [17] I. F. Perepichka, D. F. Perepichka, *Handbook of Thiophene-Based Materials: Applications in Organic Electronics and Photonics*, Wiley, Chichester, UK **2009**.

- [18] G. Barbarella, L. Favaretto, G. Sotgiu, L. Antolini, G. Gigli, R. Cingolani, A. Bongini, *Chem. Mater.* **2001**, *13*, 4112.
- [19] a) F. Wu, D. Rocca, Y. Ping, *J. Mater. Chem. C* **2019**, *7*, 12891; b) U. Bockelmann, *Phys. Rev. B* **1993**, *48*, 17637.
- [20] T. Benincori, G. Bongiovanni, C. Botta, G. Cerullo, G. Lanzani, A. Mura, L. Rossi, F. Sannicolò, R. Tubino, *Phys. Rev. B* **1998**, *58*, 9082.
- [21] a) F. D. Sala, G. Gigli, M. F. Raganato, M. Anni, D. Pisignano, R. Cingolani, L. Favaretto, G. Sotgiu, G. Barbarella, L. Antolini, *Org. Electron.* **2004**, *5*, 129; b) C. Xu, R. Ye, H. Shen, J. W. Y. Lam, Z. Zhao, B. Z. Tang, *Angew. Chem., Int. Ed.* **2022**, *61*, 202204604.
- [22] V. Wisselingh, V. D. Pol, D. Gregorio, *The Global Lepidoptera Names Index LepIndex* **2010**, 1961.
- [23] a) C.-P. Hsu, *Acc. Chem. Res.* **2009**, *42*, 509; b) F. Laquai, Y.-S. Park, J.-J. Kim, T. Basché, *Macromol. Rapid Commun.* **2009**, *30*, 1203.
- [24] M. F. Raganato, V. Vitale, F. D. Sala, M. Anni, R. Cingolani, G. Gigli, L. Favaretto, G. Barbarella, M. Weimer, A. Görling, *J. Chem. Phys.* **2004**, *121*, 3784.
- [25] a) A. Llina's, J. M. Goodman, *Drug Discovery* **2008**, *13*, 198; b) D. Erdemir, A. Y. Lee, A. Myerson, *Curr. Opin. Drug Discovery Devel.* **2007**, *10*, 746.
- [26] B. Huang, E. Glynos, B. Frieberg, H. Yang, P. F. Green, *ACS Appl. Mater. Interfaces* **2012**, *4*, 5204.
- [27] a) S. A. Ruiz, C. S. Chen, *Soft Matter* **2007**, *3*, 168; b) Y. Sun, R. Duffy, A. Lee, A. W. Feinberg, *Acta Biomater.* **2013**, *9*, 7885.
- [28] P. Veliça, C. M. Bunce, *Muscle Nerve* **2011**, *44*, 366.
- [29] H. Park, R. Bhalla, R. Saigal, M. Radisic, N. Watson, R. Langer, G. Vunjak-Novakovic, *J. Tissue Eng. Regener. Med.* **2008**, *2*, 279.
- [30] D. T. Jayaram, Q. Luo, S. B. Thourson, A. H. Finlay, C. K. Payne, *Small* **2017**, *13*, 1700789.
- [31] J. C. de Mello, H. F. Wittmann, R. H. Friend, *Adv. Mater.* **1997**, *9*, 230.
- [32] J. A. Levitt, P.-H. Chung, M. K. Kuimova, G. Yahioglu, Y. Wang, J. Qu, K. Suhling, *ChemPhysChem* **2011**, *12*, 662.
- [33] a) J. Shi, C. Tomasi, in 1994 Proc. IEEE Conf. on Computer Vision and Pattern Recognition, IEEE, Piscataway, NJ, USA, **1994**, pp. 593–600; b) B. D. Lucas, T. Kanade, in Proc. 7th Int. Joint Conf. on Artificial intelligence, IJCAI'81, ACM, New York, **1981**, pp. 674–679; c) Z. Kalal, K. Mikolajczyk, J. Matas, in 2010 20th Int. Conf. on Pattern Recognition, IEEE, Piscataway, NJ, USA, **2010**, pp. 2756–2759; d) C. Tomasi, T. Kanade, Detection and Tracking of Point Features, Carnegie Mellon University Technical Report CMU-CS-91-132, April **1991**.